

## RESEARCH ARTICLE

10.1002/2015JD024537

## Key Points:

- Spiral ascent through a stratiform riming region descent showing enhanced aggregation process signatures
- Collocated remote sensing from multiple wavelength dual polarization radar and disdrometer
- Bimodal Doppler spectra and radar signatures indicative of ice needle formation near riming regions

## Correspondence to:

S. E. Giangrande,  
sgrand@bnl.gov

## Citation:

Giangrande, S. E., T. Toto, A. Bansemer, M. R. Kumjian, S. Mishra, and A. V. Ryzhkov (2016), Insights into riming and aggregation processes as revealed by aircraft, radar, and disdrometer observations for a 27 April 2011 widespread precipitation event, *J. Geophys. Res. Atmos.*, 121, 5846–5863, doi:10.1002/2015JD024537.

Received 19 NOV 2015

Accepted 29 APR 2016

Accepted article online 5 MAY 2016

Published online 19 MAY 2016

# Insights into riming and aggregation processes as revealed by aircraft, radar, and disdrometer observations for a 27 April 2011 widespread precipitation event

Scott E. Giangrande<sup>1</sup>, Tami Toto<sup>1</sup>, Aaron Bansemer<sup>2</sup>, Matthew R. Kumjian<sup>3</sup>, Subhashree Mishra<sup>4</sup>, and Alexander V. Ryzhkov<sup>4</sup>

<sup>1</sup>Atmospheric Sciences Division, Brookhaven National Laboratory, Upton, New York, USA, <sup>2</sup>National Center for Atmospheric Research, Boulder, Colorado, USA, <sup>3</sup>Department of Meteorology, Pennsylvania State University, University Park, Pennsylvania, USA, <sup>4</sup>Cooperative Institute for Mesoscale Meteorological Studies, University of Oklahoma and NOAA/National Severe Storms Laboratory, Norman, Oklahoma, USA

**Abstract** This study presents aircraft spiral ascent and descent observations intercepting a transition to riming processes during widespread stratiform precipitation. The sequence is documented using collocated scanning and profiling radar, including longer-wavelength dual polarization measurements and shorter-wavelength Doppler spectra. Riming regions are supported using aircraft measurements recording elevated liquid water concentrations, spherical particle shapes, and saturation with respect to water. Profiling cloud radar observations indicate riming regions during the event as having increasing particle fall speeds, rapid time-height changes, and bimodalities in Doppler spectra. These particular riming signatures are coupled to scanning dual polarization radar observations of higher differential reflectivity ( $Z_{DR}$ ) aloft. Reduced melting layer enhancements and delayed radar bright-band signatures in the column are also observed during riming periods, most notably with the profiling radar observations. The bimodal cloud radar Doppler spectra captured near riming zones indicate two time-height spectral ice peaks, one rimed particle peak, and one peak associated with pristine ice needle generation and/or growth between  $-4^{\circ}\text{C}$  and  $-7^{\circ}\text{C}$  also sampled by aircraft probes. This pristine needle population gives a partial explanation for the enhanced  $Z_{DR}$  we observe near this rimed particle region. The riming signatures aloft and radar measurements within the melting level are weakly lag correlated ( $r \sim 0.6$ ) with smaller median drop sizes at the surface, as compared with later times when aggregation of larger particle sizes was believed dominant.

## 1. Introduction

To address deficiencies in the treatment of microphysical processes in cloud resolving and global climate models (GCM), there has been a growing demand for observational data sets to better constrain model parameterizations. Emphasis has been on convective life cycle and associated precipitation process studies as convective clouds carry influence across large spatial and temporal scales. Simulating cloud and precipitation processes requires improved observations to better identify the conditions wherein particular microphysical processes are active, as well as dominant. In response to the high cost associated with in situ aircraft observations, two-way interactive studies between cloud microphysical process observations and modeling have looked to draw insights from radar signatures known to be sensitive to changes in bulk or spectral particle distribution properties that may be useful for improving cloud process parameterizations [e.g., Kollias *et al.*, 2007, 2011; Kumjian and Ryzhkov, 2010, 2012; Ryzhkov *et al.*, 2011, 2013; Kumjian *et al.*, 2012; Battaglia *et al.*, 2013; Andric *et al.*, 2013; Kumjian and Prat, 2014; Kalesse *et al.*, 2016].

To better elucidate dynamical and microphysical process evolutions from shallow to deeper clouds in climate models, the U.S. Department of Energy's (DOE) Atmospheric Radiation Measurement (ARM) Climate Research Facility recently outfitted its global climate facilities with additional remote sensing capabilities [e.g., Ackerman and Stokes, 2003; Mather and Voyles, 2013]. Multifrequency profiling and dual polarization scanning radars were deployed to help bolster an ARM "supersite" climate model evaluation test bed [e.g., Stokes and Schwartz, 1994; Ackerman and Stokes, 2003; Illingworth *et al.*, 2007] at the Oklahoma Southern Great Plains (SGP) Central Facility (CF) site near Lamont, OK. These facilities were unveiled coinciding with the joint Midlatitude Continental Convective Clouds Experiment (MC3E) between DOE's ARM and the National

Aeronautics and Space Administration (NASA) Global Precipitation Measurement mission [e.g., *Hou et al.*, 2014; *Jensen et al.*, 2015a]. From 22 April 2011 to 6 June 2011, the NASA aircraft facilities complemented the heavily instrumented North Central Oklahoma region (having surface DOE ARM, NOAA Next Generation Weather Radar, and Oklahoma Mesonet equipment). This provides a unique backdrop to evaluate radar signatures and their usefulness to identify or better constrain several key precipitation processes coincident with aircraft observations.

This study documents an early MC3E event observed during weak convection and widespread precipitation on 27 April 2011. Radar and surface disdrometer observations were supported by aircraft measurements, including a spiral ascent and descent through the depth of the cloud including the melting layer. Although aircraft data sets within stratiform regions and melting layers are not uncommon [e.g., *Stewart et al.*, 1984; *Willis and Heymsfield*, 1989; *Heymsfield et al.*, 2015], spiral data sets that provide additional reference for multiwavelength dual polarization radar observations of the ice and mixed-phase parts of the clouds are typically unavailable [e.g., *White et al.*, 2002; *Sassen et al.*, 2005]. The aircraft spirals on this day were fortuitous and provide a valuable anchor to help explain the microphysical process complexity we observe around several key instances. During the spiral ascent and descent, the aircraft intercepted different types of snow particles with various degrees of riming that were simultaneously observed with a number of ground-based remote sensing instruments. These sensors include high-resolution vertically pointing Ka-band Doppler radar (35 GHz), the 915 MHz wind profiler, and scanning dual polarization radar operating at C band (5.4 GHz).

This study aims to capitalize on the available aircraft and multiwavelength radar observations collected during this event to investigate radar capabilities for recognizing riming processes, aggregation processes, and possible transitions from riming to aggregation favorable conditions. A secondary goal is to investigate the information contained within shorter-wavelength radar Doppler spectra and profiling radar data sets within precipitation often overlooked in cases having complementary aircraft and surveillance dual polarization radar observations. The paper is outlined as follows. An overview of the event and the associated observational considerations is presented in section 2. The event is analyzed using a multisensor observational approach in section 3. Key findings are summarized in section 4.

## 2. The 27 April Event (Data Set and Methodology)

The 27 April 2011 event was associated with an elevated front stationed across North Central Oklahoma (approximately 350 m mean sea level (msl)). ARM instrumentation captured multiple convective bands passing over the SGP CF evidenced by lower-level (below 3 km msl) vertical air motions exceeding  $3 \text{ m s}^{-1}$  as estimated by radar wind profiler (RWP) measurements [e.g., *Giangrande et al.*, 2013]. These bands were followed by a transition to widespread stratiform precipitation with continued weak convection to the south and east. The University of North Dakota (UND) Citation aircraft (hereafter, Citation) was launched after 08:00 UTC targeting operations in the less turbulent stratiform conditions. During aircraft operations, no vertical air motions exceeding  $3 \text{ m s}^{-1}$  were sampled by the Citation or by the RWP.

The Citation performed stepped leg patterns over the SGP CF through the stratiform region between 08:00 UTC and 10:00 UTC remaining within 40 km from the SGP CF throughout the sampling period (Figures 1 and 2). Cloud-based winds obtained from 3-hourly MC3E radiosondes were northerly during the event, shifting to northwesterly as the surface low tracked eastward [e.g., *Jensen et al.*, 2015b]. Aircraft probe measurements along the flight legs indicated larger aggregates, with supercooled liquid droplet signatures at  $-10^{\circ}\text{C}$  (4 km msl). When the aircraft descended to  $-4^{\circ}\text{C}$  (3 km msl), needles and rimed particles were sampled between 09:36 UTC and 09:48 UTC [e.g., *Kumjian et al.*, 2016]. Otherwise, larger aggregates ( $>10 \text{ mm}$ ) were observed with the largest aggregates sampled within deeper cells east of SGP CF. The Citation aircraft returned to the SGP CF by 10:32 UTC to perform upward and downward spirals (from approximately 1.2 km to 4.8 km msl), which are in the focus of our investigation (approximately 10:35 UTC to 11:08 UTC).

### 2.1. The MC3E Radar Data Set

One key ground-based instrument for this study was a vertically pointing 35 GHz Ka-band Zenith Radar (KAZR, Figures 1a–1c) [e.g., *Clothiaux et al.*, 2000; Atmospheric Radiation Measurement (ARM), 2011; *Kollias et al.*, 2014]. We capitalize primarily on the estimates of the mean Doppler velocity and the moments of

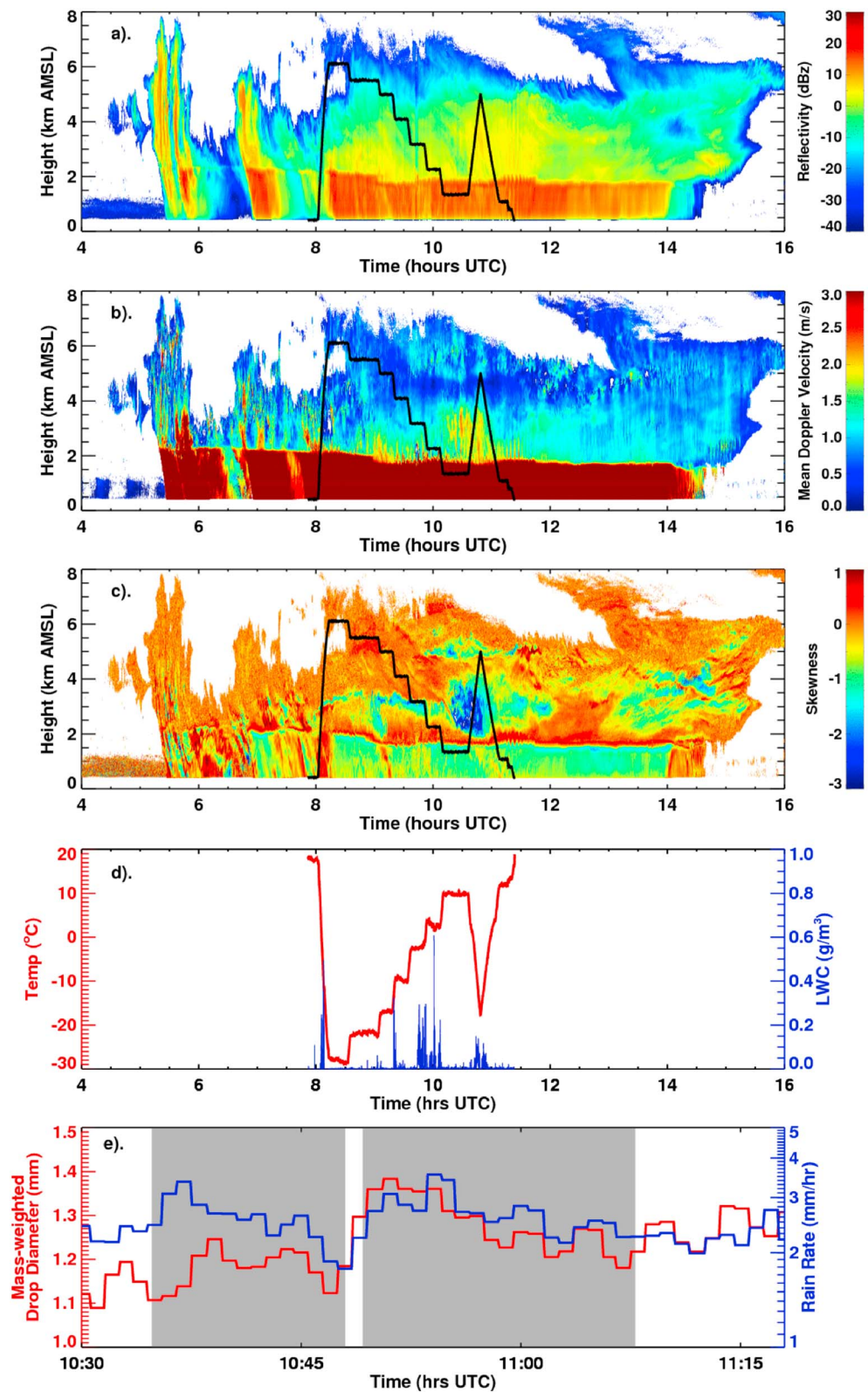


**Figure 1.** Time-height plots from the 27 April 2011 event for (a) KAZR reflectivity factor, (b) KAZR mean Doppler velocity, (c) KAZR skewness, (d) Citation temperature and CDP probe liquid water content, and (e) spiral close up for disdrometer median diameter and rainfall rate. Citation altitude overlaid on each KAZR image in black but may reflect a spatial position only to within 40 km of the SGP CF. Shaded regions in Figure 1e represent specific spiral windows.

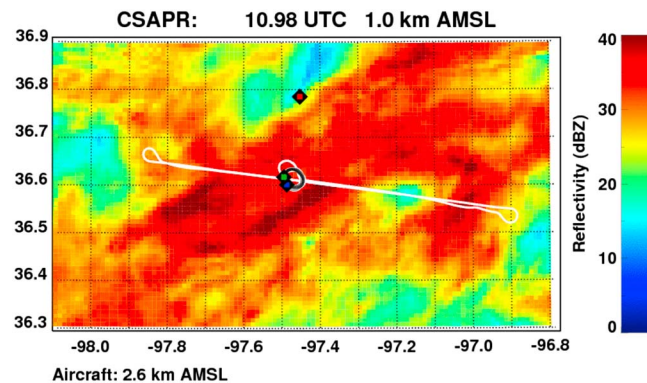


**Figure 2.** CSAPR constant altitude (1 km) Reflectivity Factor  $Z$  image from the 27 April 2011 event during the spiral. The red diamond is the CSAPR location. The blue diamond is the SGP CF. Green diamond and its track represents aircraft location and prior flight path.

Doppler spectra (such as spectral skewness) [e.g., Luke and Kollias, 2013] that are immune to attenuation in rain, wet radome, and radar miscalibration (Figures 1b and 1c). Spectral skewness is defined as “negative” when the Doppler spectrum deviates from a Gaussian shape to include a left side tail. If a Doppler spectrum is initially a Gaussian, the onset of negative skewness may be interpreted as an addition of slower falling (i.e., with lower downward Doppler velocities) particles. For example, Figure 1c highlights a sizable region having negative skewness embedded in the stratiform precipitation around our

aircraft spirals. Additionally, Doppler spectral density waterfall plots (spectrograms) are examined to identify bimodal spectra associated with different particle species in the radar resolution volume. The spectrograms are generated directly from the individual KAZR Doppler spectra with no additional smoothing or adjustments (256-point fast Fourier transform, 20 spectral averages for the native 4 s temporal, 30 m spatial resolution). Readers may also consult Lhermitte [1988], Kollias *et al.* [2011], Giangrande *et al.* [2010, 2012], and Oue *et al.* [2015] among many others on various issues and methodologies of the cloud radar analysis.

Profiling observations at longer wavelengths were available from the 915 MHz radar wind profiler (RWP) collocated with the KAZR. This RWP was reconfigured for deeper precipitation modes and collected data similar to an S-band radar profiler [e.g., Bellon *et al.*, 1997; ARM, 2009; Williams, 2012; Giangrande *et al.*, 2013]. The RWP beam width is large ( $6^\circ$ ); however, the vertical and temporal resolution (200 m and 5 s, respectively) was consistent with KAZR.

A surveillance 5.4 GHz (5 cm wavelength) dual polarization C-band Scanning ARM Precipitation Radar (CSAPR) located approximately 20 km north of SGP CF was also utilized. The CSAPR data have  $1^\circ$  azimuthal resolution and 100 m range resolution. The CSAPR radar reflectivity  $Z$  and differential reflectivity  $Z_{DR}$  were calibrated to the accuracy of 2 dBZ and 0.2 dB, respectively, using standard calibration techniques [e.g., ARM, 2010; Giangrande *et al.*, 2013, 2014b]. Differential reflectivity is a key polarimetric variable that provides information about particle size, shape, orientation, density, and phase composition. An example of Constant Altitude Plan Position Indicator (PPI) (CAPPI) of  $Z$  measured by CSAPR at the height of 1 km with the Citation track overlaid is shown in Figure 2.

One-minute rainfall rate and mass-weighted drop diameter ( $D_m$ ) measurements are obtained from the ARM impact disdrometer [Joss and Waldvogel, 1967; ARM, 2006; Giangrande *et al.*, 2014a], (Figure 1e).  $D_m$  is selected because it is a relatively robust parameter defined as the ratio of the fourth moment to the third moment of the drop size distribution [e.g., Bringi *et al.*, 2002, 2003]. Discrepancies in  $D_m$  magnitudes are observed when comparing with nearby video disdrometers [e.g., Tokay *et al.*, 2013]. However, linear correlations between colocated disdrometer records are high ( $r \sim 0.9$ ), providing confidence in disdrometer time series behaviors for qualitative comparisons in this study.

## 2.2. Aircraft Instrumentation

The Citation aircraft was outfitted with cloud microphysical and particle imaging probes for standard meteorological state, vertical air motion, cloud liquid water content (LWC), and total water content (TWC) estimates using particle measuring systems (PMS) King and Sky Tech Research, Inc., Nevzorov probes. The instrument package also included probes for particle types, sizes, and distributions. Relative humidity (RH) with respect to liquid water and relative ice supersaturation were computed using the measured temperature and dewpoint temperature from a chilled mirror hygrometer.

Ice particle size distribution (PSD) information was obtained from several probes. The ice crystal images presented in this study come from the Droplet Measurement Technologies (DMT) Cloud Imaging Probe (CIP) that provides high-resolution ice crystal images in the size range of 100  $\mu\text{m}$  to 1 mm at 25  $\mu\text{m}$

resolution. A PMS two-dimensional cloud (2D-C) optical array probe [Knollenberg, 1981] covered a similar size range with 30  $\mu\text{m}$  resolution. The nominal sample volume of the 2D-C is 4.88 L per 100 m of flight path for hydrometeors  $\geq 125 \mu\text{m}$ . Larger hydrometeors were sampled by a SPEC High Volume Precipitation Spectrometer (HVPS-3) probe having a resolution of 150  $\mu\text{m}$  [e.g., Lawson *et al.*, 1998], which measured particles from 1 mm to 2 cm in diameter. The HVPS-3 sample volume is 320  $\text{L s}^{-1}$  at 100  $\text{m s}^{-1}$ . A DMT Cloud Droplet Probe (CDP) is also used to sample small particles (supercooled liquid droplets and small ice particles), providing number concentration measurements for sizes  $< 50 \mu\text{m}$ . The presence of supercooled liquid water was also informed by a Rosemount Icing Detector [Baumgardner and Rodi, 1989]. These signatures are most reliable for temperature conditions colder than  $-3^\circ\text{C}$  [e.g., Wang *et al.*, 2015]. Additional Citation instrument uncertainty ranges and discussions on the probe suite available during MC3E are found in Wang *et al.* [2015].

The aircraft data analysis includes estimation of an area ratio (AR) parameter [e.g., Heymsfeld and Westbrook, 2010] defined as the ratio of the projected area of the two-dimensional ice crystal image to the area of its circumscribing circle. AR values near unity are associated with spherical particles, whereas lower AR values may be attributed to nonspherical particles. The AR estimates presented in this study were calculated from the HVPS-3 alone and not based on 2D-C or CIP images. The AR values use fully and partially imaged particles; however, the interpretations for this event would be similar if comparing these calculations to the calculations performed using only fully captured particles.

### 3. Observations and Interpretation for the 27 April Event

This section presents the observations and an analysis of the aircraft and ground data sets collected on 27 April 2011 during the upward and downward spirals (herein Spiral 1, 10:35 to 10:48 UTC, and Spiral 2, 10:49 to 11:08 UTC). Citation ascent and descent speeds were approximately 2  $\text{m s}^{-1}$  [e.g., Heymsfeld *et al.*, 2015] during the spiral observations considered in section 3.1. Sections 3.2 and 3.3 introduce and interpret the ground-based observations relative to the aircraft insights discussed in section 3.1 to determine the extent these ground resources are informative for identifying processes including riming and aggregation.

#### 3.1. Citation Spirals

##### 3.1.1. Citation Spiral Probe Observations

Citation spirals provide the aircraft in situ evidence for possible riming processes and the transitions from riming-favorable conditions to the aggregation conditions as suggested by radar during the 27 April event. The Citation data sets along the spirals are illustrated in Figures 3–7. The interpretation for these spiral probe observations follows in section 3.1.2.

Figures 3 and 4 show Spiral 1 and Spiral 2 histograms for particle size distribution (PSD) information. These histograms reflect the HVPS-3 number concentration (Figures 3a and 4a) as well as the HVPS-3 AR parameter measurements as described by section 2.2 (Figures 3b and 4b). The aircraft distance from the SGP CF location and the temperature profiles associated with the spirals are also plotted. Additional PSD information on the changes observed between Spiral 1 and Spiral 2 is in Figure 5. This figure presents the combined PSD profile behavior of each spiral, as constructed by merging the CIP probe (for particles with diameters in the range of 0.1–1.0 mm) and the HVPS-3 probe data sets (for particles larger than 1 mm). The combined PSDs are fit to an exponential functional form, with the slope ( $\lambda$ ) and intercept ( $N_0$ ) parameters from those PSD exponential fits (profiles as a function of height) plotted in Figure 5. For all images that overlay spiral measurements, Spiral 1 (Spiral 2) data sets are plotted using blue (red) colors.

Additional Citation probe observations along Spiral 1 and Spiral 2 are located in Figures 6 and 7, accompanied by aircraft temperature traces in the rightmost panels. Figure 6 plots the LWC as estimated by the (Figure 6a) King and (Figure 6b) CDP probes, as well as TWC estimates in Figure 6c. Figure 7 presents the comparisons of the (Figure 7a) spiral relative humidity (RH) (solid lines) and ice supersaturation (dashed lines, vapor pressure,  $e$ , divided by an estimate for the saturation vapor pressure over ice,  $e_i$ ) and the (Figure 7b) vertical air motion as estimated by Citation [e.g., Khelif *et al.*, 1999]. The output of the Rosemount probe frequency is plotted in Figure 7c.

From an overarching perspective, Spiral 1 PSDs generally contain lower concentrations of large ( $> 1 \text{ mm}$ ) ice as compared to Spiral 2 (Figures 3a and 4a). This observation is also supported by PSD parameter estimates

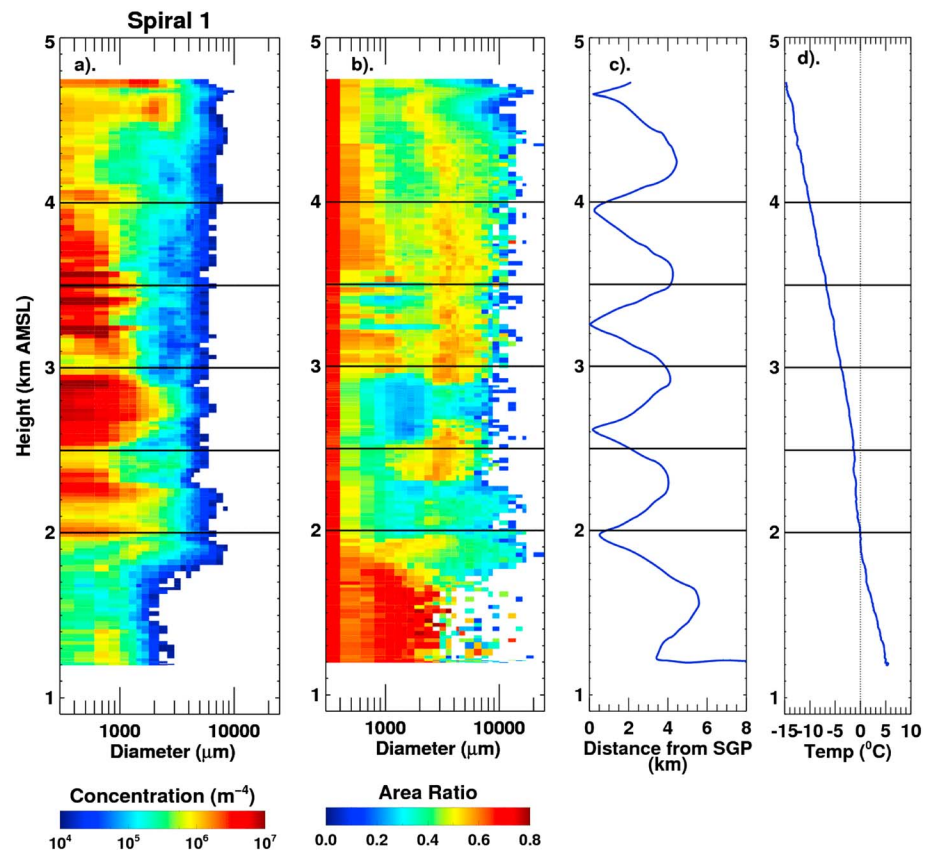


**Figure 3.** Upward spiral (Spiral 1) histograms for Citation (a) HVPS-3 number concentration and (b) HVPS-3 AR parameter measurements with (c) UND Citation spiral distance from the SGP CF and (d) temperature measurements.

found in Figures 5a and 5b, as reflected by lower values for  $\lambda$  coupled with similar or lower values of  $N_0$ . The AR distributions along Spiral 1 indicate additional spherical shapes for 2 mm – 7 mm particles, characteristic of more heavily rimed particles compared to Spiral 2 (Figures 3b and 4b).

An immediate focal point for spiral comparison purposes is in the regions above 3.5 km, wherein both spirals indicate elevated LWC, as based on the measurements from multiple Citation probes (Figures 6a and 6b), as well as possible upward vertical motions (Figure 7b). The measurements along Spiral 1 indicate higher LWC and possible stronger upward motions, but one may exhibit caution when interpreting probe measurements and these vertical velocity observations in particular since the observed differences (e.g., to within  $1 \text{ ms}^{-1}$ ) are within the uncertainty ranges typically associated with these probes [e.g., *Khelif et al.*, 1999; *Rosenberg et al.*, 2012; *Guyot et al.*, 2015; *Wang et al.*, 2015]. To accompany LWC differences, a more persistent and potentially reliable distinction between the spirals is found in the RH traces (Figure 7a). Spiral 1 RH values indicate supersaturation with respect to water (thus supersaturation with respect to ice), whereas a brief time later, the air along Spiral 2 is supersaturated with respect to ice, but subsaturated with respect to water. These particular RH discrepancies also persist throughout most of the duration of the respective spirals. To altitudes below 3 km, Spiral 2 maintains larger particle sizes and lower AR values, but both spirals support similar relative changes to PSD behaviors (Figure 5) for temperatures greater than  $-3^\circ\text{C}$ . These PSD changes include decreases in the slope parameter with corresponding decreases in the total number concentration.

Once the spirals are within the melting layer, the previous study by *Heymsfield et al.* [2015] well summarizes key melting features for MC3E events. For this 27 April event, the spirals exhibit similar temperature profiles, with higher RH values near the melting level. These higher RH values imply that melting should commence close to  $0^\circ\text{C}$  in both cases. This is confirmed by probe images that indicate particle melting near 2.1 km msl. These behaviors should be observable from radar-based properties that follow.

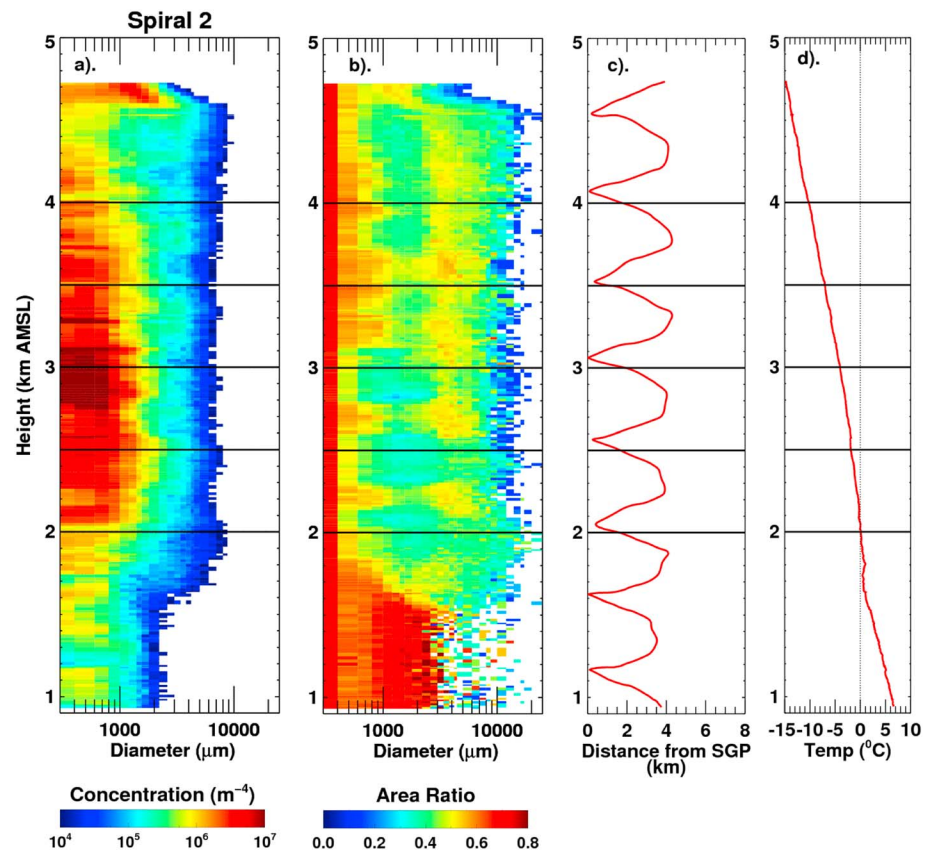


**Figure 4.** As in Figure 3 but for the downward spiral, Spiral 2.

### 3.1.2. Spiral Measurement Probe Interpretation

One important initial take away from these spiral observations is that Citation probe measurements suggest the presence of supercooled liquid water along Spiral 1. This is a necessary ingredient for riming and when establishing confidence in pinpointing riming regions with radar. Both spirals indicate the presence of rimed particles on probe imagery (Figure 8), while AR arguments provide additional evidence for riming near these spirals. The Spiral 1 observations also indicate heightened RH values that are supersaturated with respect to water, as well as elevated LWC from multiple sensors including the CDP probe that samples sizes that include supercooled liquid drops. The observed drop in Rosemount probe frequency (Figure 7c) may also be interpreted under these contexts to suggest a supercooled liquid water signal between 3.5 km and 3.7 km ( $-8^{\circ}\text{C}$ ). The corresponding supercooled water signatures are less pronounced along Spiral 2; therefore, one may have less confidence in interpreting available Rosemount probe behaviors that suggest possible light icing from 3.7 km down to 2.7 km ( $-8^{\circ}\text{C}$  to  $-3^{\circ}\text{C}$ ).

Consolidating these behaviors along the upper spiral portions, one may start by considering that the cooling associated with regions having weak upward vertical motions (consistent with Citation measurements in Figure 7b) can be conducive for increased RH and subsequent liquid droplet production. Ice crystals available under such conditions act to deplete water vapor excess through deposition, or new particle formation, whereas the available liquid water may be depleted by riming. Because the air along Spiral 1 is saturated with respect to water, the higher LWC and constant TWC measurements may indicate relatively lower ice water contents as compared to Spiral 2. Therefore, the higher LWC along Spiral 1 may lead to cloud droplet formation and/or riming that may dominate over deposition. This particular interpretation seems to also align with observed increases in particle AR (spherical, rimed particles, Figure 3b). Meanwhile, Spiral 2 observations display a pronounced shift toward larger particles, accompanied by lower RH ( $\sim 98\%$ ), lower LWC, and increases in the TWC below 3.5 km msl. This may suggest that Spiral 2 atmospheric conditions are those that follow an influx or impulse toward larger particles aloft and subsequently favorable conditions for sustaining larger, less rimed, and less spherical (lower AR) ice crystals ( $>8$  mm diameter, Figure 4b).

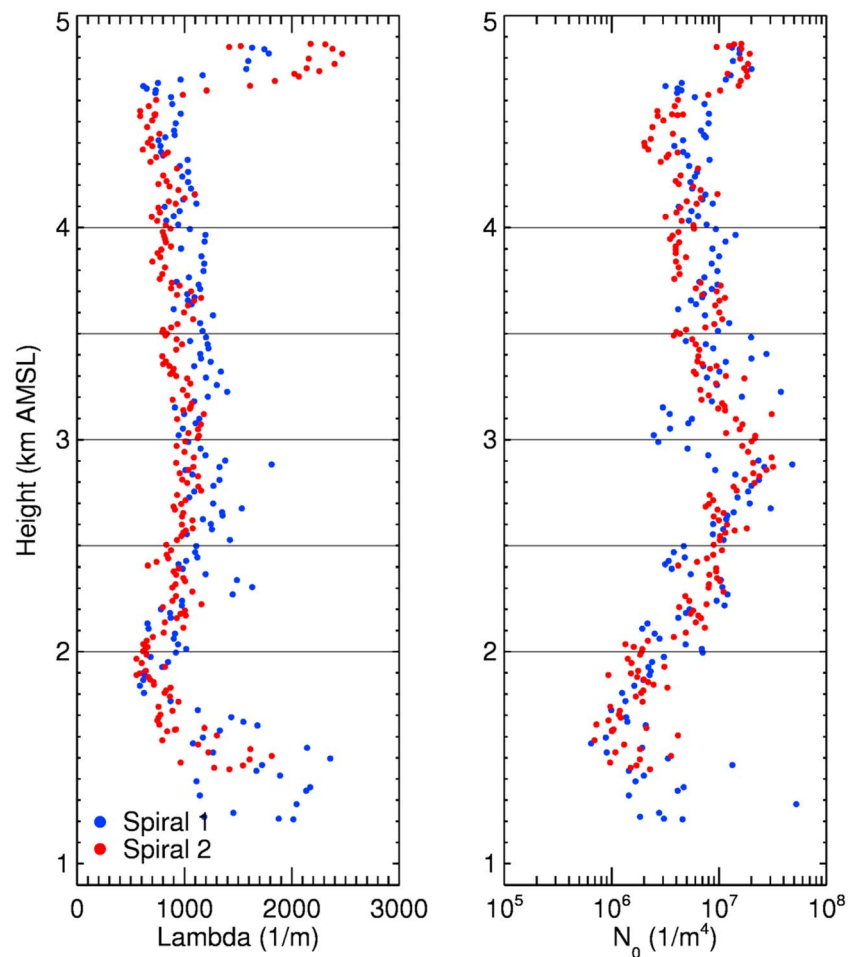


**Figure 5.** Exponential fit slope ( $\lambda$ ) and intercept ( $N_0$ ) parameter profiles to the combined PSD information from merged CIP and HVPS-3 probe data sets along the upward (blue) and downward (red) spiral.

Exploring spiral contrasts and implications to lower altitudes, it is important to highlight that riming and aggregation may coexist along the same atmospheric columns (time-height) sampled by an aircraft spiral or profiling radar. This is likely the situation for an evolving system and appears to be echoed by the profile observations available during this study. To altitudes below 3 km, both spirals show similar PSD behaviors (Figure 5) that indicate the onset of aggregation processes for temperatures greater than  $-3^{\circ}\text{C}$ . The changes in the slope parameter below approximately 2.7 km (decreases) suggest that larger-sized particles are formed when ice particles collide (total number concentration also decreases). Moreover, while Spiral 1 conditions aloft are those we interpret as favorable for riming processes (smaller and/or more spherical particles), both spirals qualitatively indicate similar aggregation process responses at altitudes below 2.7 km. However, the PSDs entering these levels are not similar, with differences in the presence of larger particle sizes that persist to lower altitudes (Figures 3–5). In particular, these differences should impact the signatures associated with aggregation processes as viewed by radar that are more sensitive to the presence of larger particles.

### 3.1.3. Additional Spiral Observations and Interpretation: Ice Needles

In addition to available profile evidence for riming and aggregation processes, Figures 3b and 4b reveal detailed bulk AR value contrasts specific to the 1–2 mm size range. Spiral 1 exhibits pronounced lower (0.2–0.4) AR values below 3.5 km. The aircraft-observed temperature and ice supersaturation conditions at these altitudes are consistent with needle-like crystal habits [e.g., Bailey and Hallett, 2009]. Provided available ice nuclei or embryonic ice, observed ice supersaturation would favor nucleation and/or rapid growth of new ice crystals [e.g., Kobayashi, 1961; Fletcher, 1962; Knight, 2012]. The favorable conditions are only found along Spiral 1. In contrast, measurements along Spiral 2 reveal less favorable conditions and higher AR values

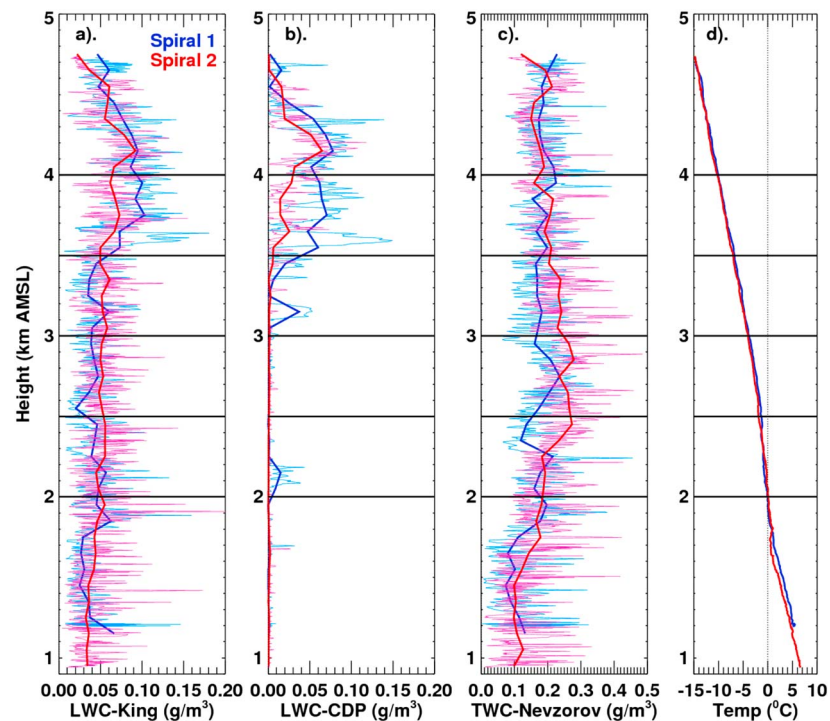


**Figure 6.** Citation aircraft profile observations for LWC from the (a) King and (b) CDP probes, the (c) TWC and the (d) temperature for the upward (Spiral 1, blue) and downward (Spiral 2, red) spiral.

(more spherical) for these needle-sized ranges. Citation images confirm the presence of rimed particles and pristine ice needles along Spiral 1 near these altitudes (Figure 8a). Rimed particles and ice needles are also observed along Spiral 2 (Figure 8b). Interpretation of instantaneous images and concentrations is not straightforward because of the variability in the Citation position and associated representativeness for narrow probe capture capabilities. However, we typically find that the needles and other particles observed along Spiral 1 are in a more pristine state. Later Spiral 2 images tend to indicate additional weak riming, which may provide one possible clue for the higher AR values specific to these size ranges.

Needle formation at these altitudes is an interesting microphysical anchor point because ice nuclei are rare for temperatures warmer than  $-10^{\circ}\text{C}$  [e.g., Zawadzki *et al.*, 2001]. As will be discussed in section 3.2, bimodal KAZR spectra exhibiting negative skewness (Figure 1c) are observed for several hours around 3 km. This bimodality is consistent with new ice needle formation and/or growth. Heterogeneous or contact nucleation explanations for this prominent needle activation are unlikely based on ice nuclei scarcity and the time over which these new spectral ice needle signatures are observed.

One possible mechanism of new ice crystal formation wherein ice nuclei are thought to be in a short supply is condensation-freezing nucleation. This requires excess water vapor to preferentially form droplets in environments supersaturated with respect to liquid water, (i.e., on soluble cloud condensation nuclei) that later or immediately freeze in a sequential process [e.g., Fukuta and Schaller, 1982]. This process favors higher ice nucleation rates for lower temperatures and/or high ice supersaturation, conditions that were available along Spiral 1, perhaps less favorable along Spiral 2.

Given possible riming conditions we argue for this event, ice multiplication by ice particle fracturing during ice-graupel collisions may also be responsible for embryonic ice [e.g., Takahashi *et al.*, 1995]. Another possibility is the Hallett-Mossop secondary ice generation within the conditions found near riming regions [e.g., Hallett and Mossop, 1974; Heymsfield and Mossop, 1984; Heymsfield and Willis, 2014]. The signatures associated with riming and rapid LWC depletion are observed between  $-10^{\circ}\text{C}$  and  $-5^{\circ}\text{C}$  (roughly 3.4 km to 4 km msl). These ranges overlap with the temperatures required for this mechanism to be active ( $-3^{\circ}\text{C}$  to  $-8^{\circ}\text{C}$ ). As in Heymsfield and Willis [2014], the most pronounced pristine needle images for this event are obtained in rather weak updrafts ( $<1\text{ m s}^{-1}$ ) with temperatures greater than  $-7^{\circ}\text{C}$  and  $\text{LWC} < 0.10\text{ g m}^{-3}$  (e.g., Figures 6 and 7). For the above

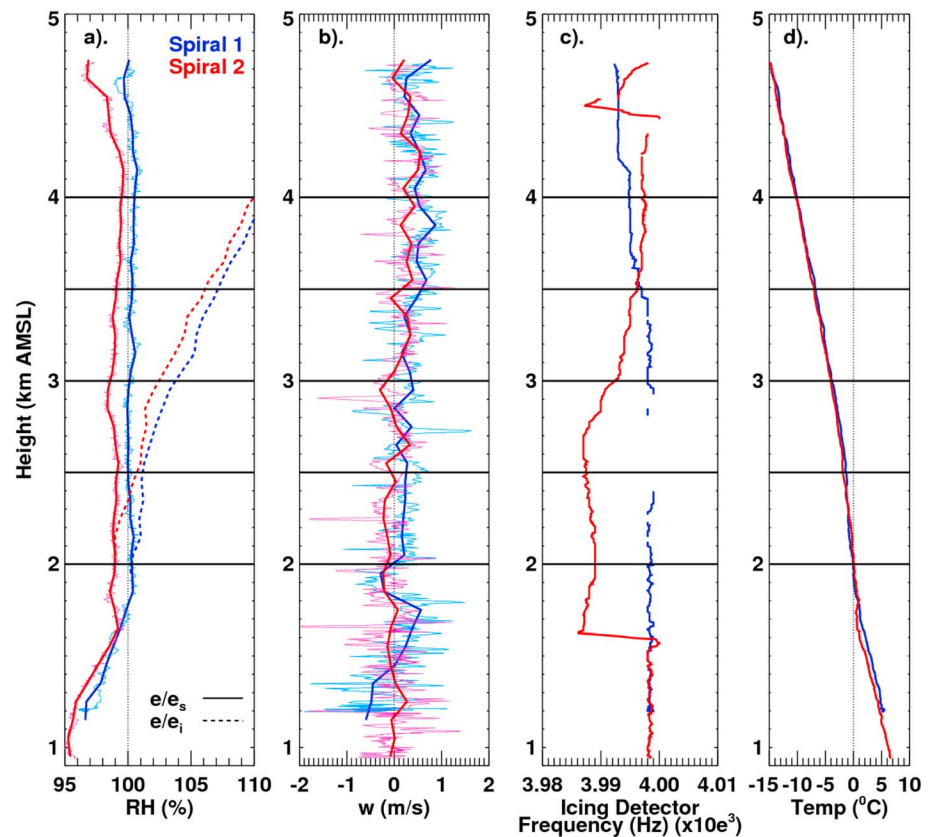


**Figure 7.** As in Figure 6 but for aircraft profile observations of (a) RH and ice supersaturation, (b) vertical velocity, (c) Rosemount probe frequency, and (d) temperature.

explanations, horizontal transport of embryonic ice from generation regions would seem to be necessary to help explain additional regions exhibiting bimodal spectra (associated with a secondary ice peak) observed near 3 km msl during most of the event.

### 3.2. ARM SGP Profilers and Disdrometer

#### 3.2.1. ARM SGP Profiling Observations

ARM SGP profiling and surface disdrometer observations are investigated to align Citation analyses from section 3.1 with potential microphysical process signatures. For column radar observations, we make use of vertical profiles of the KAZR mean Doppler velocity (Figure 9a), spectral skewness (Figure 9b), and the reflectivity factor  $Z$  from the longer wavelength RWP (Figure 9c). The KAZR copolar and cross-polar Doppler spectral density waterfall spectrums are plotted in Figures 10 and 11 for Spirals 1 and 2, respectively. For the radar data in Figures 9–11, these data sets are plotted in an attempt to align with an along-track aircraft viewpoint. That is, we select the nearest radar estimate (KAZR/RWP radar moment or Doppler spectra) in time-height to the Citation position. ARM surface disdrometer time series observations for the rainfall rate and mass-weighted drop diameter are as located in Figure 1d.

Near spiral apex ( $\sim 4$  km), KAZR spectrums indicate a very narrow, slow-falling Doppler spectral behavior typical of ice crystals on copolar and cross-polar returns (Figures 10 and 11). At these altitudes, the corresponding RWP  $Z$  values along Spiral 2 are often 2–3 dBz higher than along Spiral 1 (Figure 9c), whereas minor differences are observed for KAZR  $Z$  values (not shown). However, Spiral 1 KAZR spectrums and associated higher-order moments such as Doppler spectra skewness (Figure 1c and Figure 9b) show rapid changes at altitudes between 3 km and 4 km, including substantial increases in spectral velocity signatures consistent with faster falling, higher density rimed particles (e.g., Doppler spectra shifting toward the right in Figure 10). In contrast, the corresponding Spiral 2 profiles and spectrums at these altitudes demonstrate

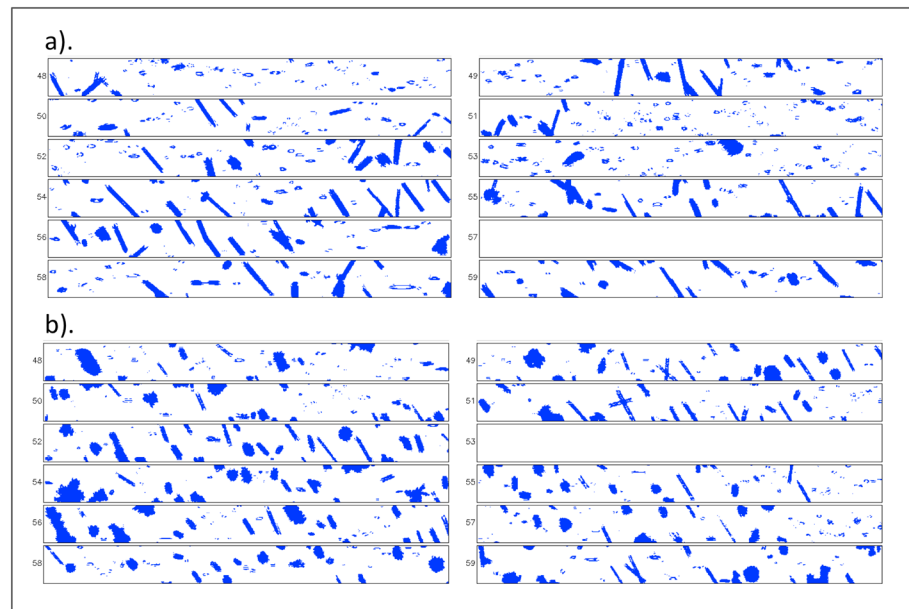


**Figure 8.** Citation CIP probe image captures from approximately  $-5^{\circ}\text{C}$  for (a) Spiral 1 and (b) Spiral 2. The width of each strip is 1.6 mm.

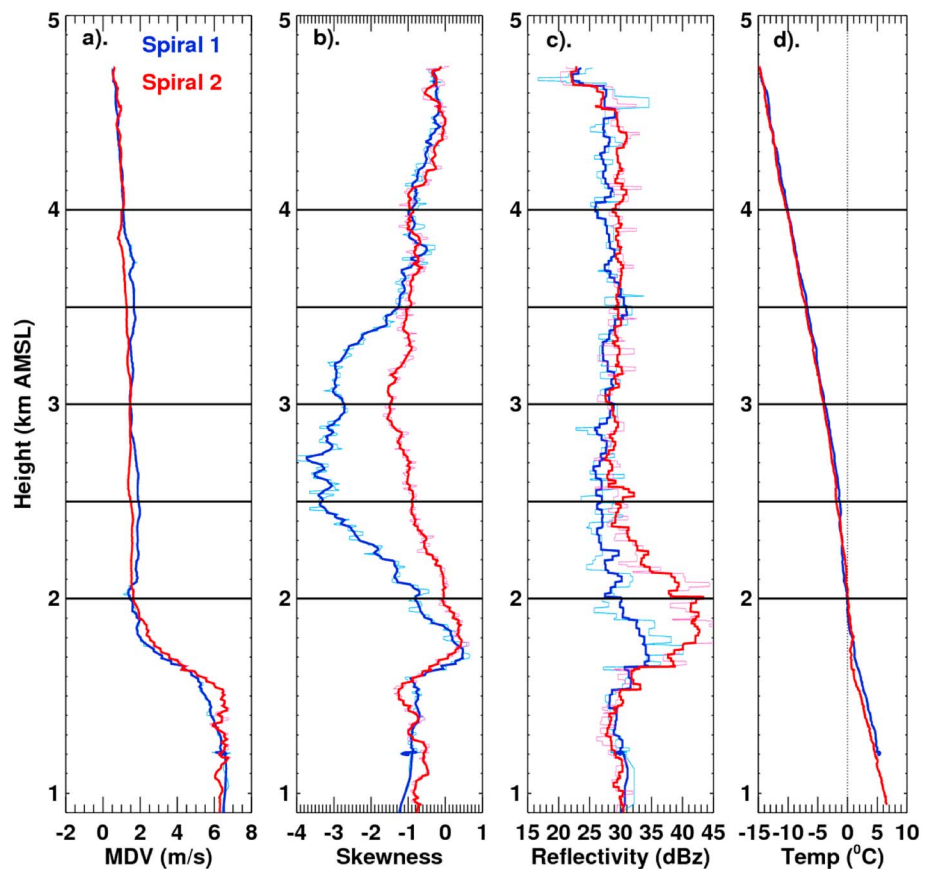


**Figure 9.** Along-track (a) KAZR mean Doppler velocity, (b) KAZR Doppler spectral skewness, (c) RWP Z profiles, and (d) corresponding Citation temperature.

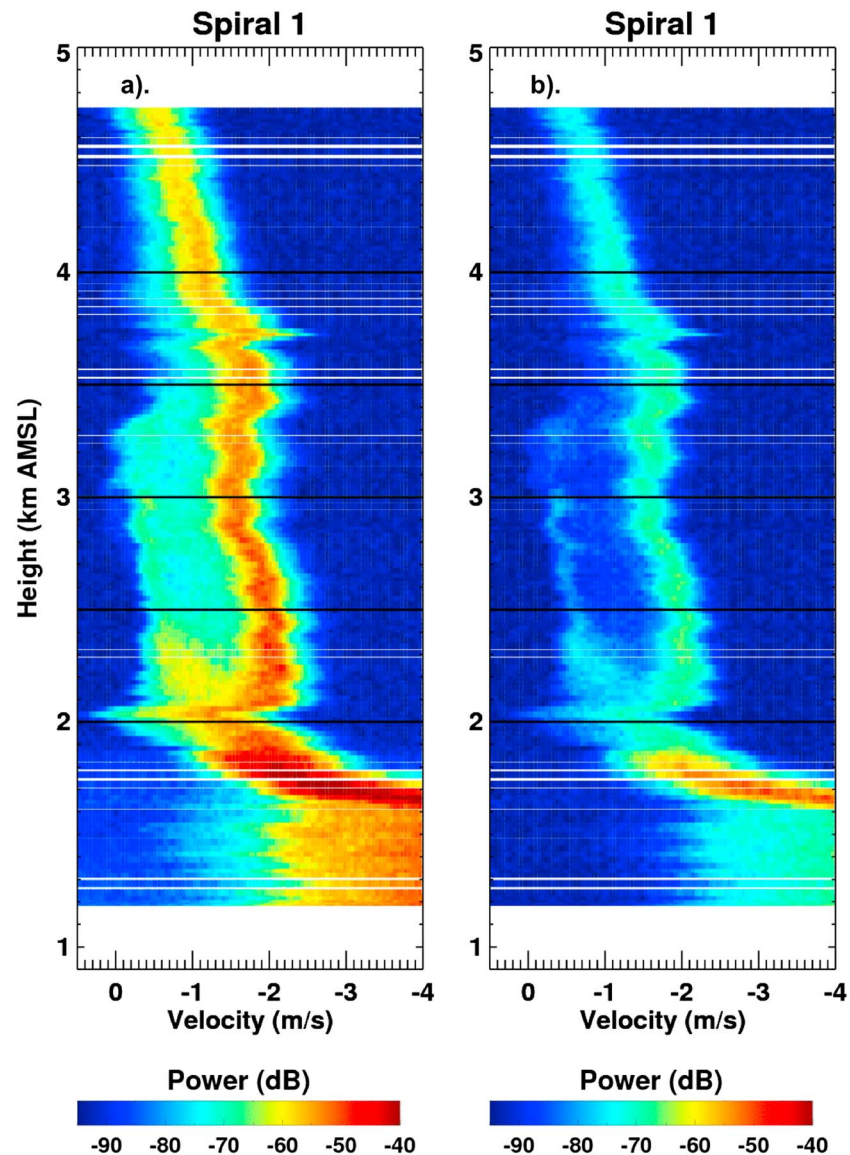


**Figure 10.** Upward spiral (Spiral 1) spectrograms for (a) “along-track” KAZR Doppler copolar and (b) cross-polar Doppler spectra.

negligible changes with height. Peak spectral velocity values increase toward the surface, from  $1 \text{ m s}^{-1}$  at 4 km msl to  $2 \text{ m s}^{-1}$  ( $1.5 \text{ m s}^{-1}$ ) at 3.5 km for Spiral 1 (Spiral 2).

Below 3 km, radar properties along Spiral 2 begin to deviate, with the RWP Z values increasing near 2.5 km (Figure 9c) consistent with traditional radar bright band and aggregation process signatures. At the surface, disdrometer  $D_m$  values (Figure 1e) are at a relative minimum (1.12 mm–1.23 mm) during Spiral 1, whereas surface  $D_m$  values throughout the later downward spiral period are higher ( $>1.25 \text{ mm}$ ). The most pronounced feature in the disdrometer time series is the sharp increase in the surface  $D_m$  values and rainfall rates after 10:50 UTC.

### 3.2.2. Profiling Instrument Interpretation Supported By Spirals

It is instructive to investigate ground-based profiling observations nearest to spiral apex first ( $\sim 4 \text{ km}$ ) then work downward in altitude to explore for prominent radar properties, contrasts, and insights into possible riming processes suggested aloft. Because the KAZR wavelength is small as compared to the larger snowflake diameters as previously indicated by Citation (e.g., Figures 3–5), KAZR measurements are less sensitive to these snowflakes. Accordingly, this explains why we may not directly detect a significant difference in the

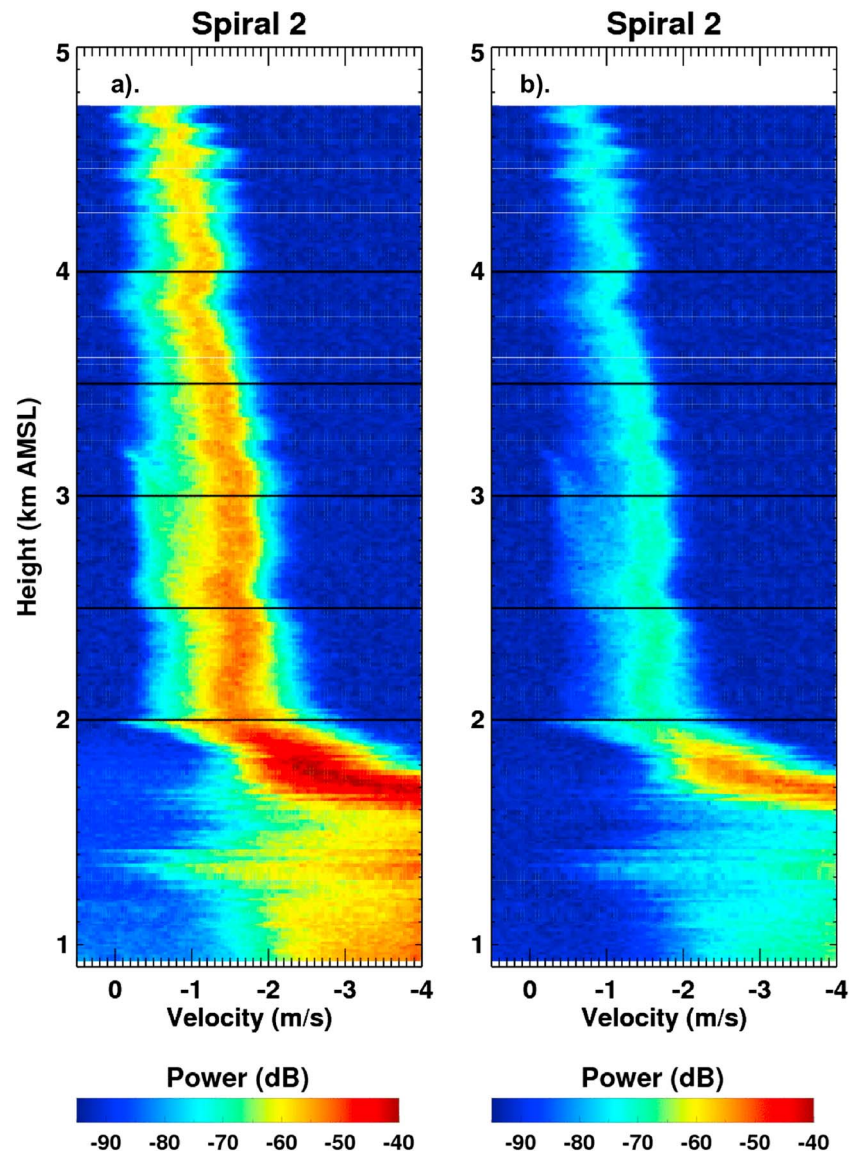


**Figure 11.** As in Figure 10 but for the downward spiral, Spiral 2.

KAZR observations between the spirals at higher altitudes  $>4$  km, despite evidence for larger (2–7 mm) particles along Spiral 2 only a brief time later (e.g., Figures 4 and 5). These issues may be better informed by the collocated RWP measurements (Figure 9c) for this case. Since the Citation consistently observes larger particles down to the melting layer along Spiral 2 (e.g., Figure 5), the higher RWP Z values along the entire profile in Figure 9c, and at these altitudes in particular, are in good agreement.

A positive confirmation for radar capabilities is found with the strong contrasts in the profiling radar-based observations coincident with the Citation locations indicating possible supercooled liquid water and riming contrasts (3.5 km to 4 km). Overall, Spiral 1 KAZR spectrograms strongly indicate these locations as rimed particle and riming (consistent time-height changes) regions, with continued signatures of rimed particle presence to lower altitudes. Unlike the altitudes aloft, the longer-wavelength RWP is apparently less sensitive to the rimed particles in these regions, exhibiting only a slight increase in Z and mean Doppler velocity along Spiral 1 (Figure 9c, 3.5 km to 4 km). Again, the bulk RWP Z measurements are most likely dominated by the presence and/or absence of additional larger snowflakes.

The increase in RWP Z below 2.5 km (Figure 9c) is noteworthy and appears consistent with traditional radar signature support for aggregation processes beginning to dominate as temperatures approach

–1.5°C to –2°C. These regions are also consistent with the Citation arguments for aggregation onset (~2.7 km). Approximately half of the 14 dBZ bright band Z enhancement (relative to regions prior to aggregation onset) observed by the RWP along Spiral 2 is above the melting level, with a 6–7 dBZ enhancement within the melting layer. As discussed in section 3.1, despite an absence for RWP Z aggregation signatures, the Citation observations support that aggregation are also taking place along Spira1 1 (Figure 5). One interpretation is that smaller particles are aggregating along Spiral 1; thus, the traditional longer-wavelength radar-based aggregation signatures are masked by the size of those aggregates as compared to the modest sized, rimed particles. In Figures 9 and 10, Doppler spectragrams near the bimodality and changes to spectral skewness may still be informative on aggregation when the traditional radar moments are not.

As modeled by Ryzhkov *et al.* [2008] and Kumjian *et al.* [2016], faster falling rimed particles increase the depth over which traditional radar bright band enhancements occur as these particles fall further before total melting. Additionally, Kumjian *et al.* [2016] show that rimed particles entering the melting layer also tend to force a depression in the height of apparent melting layer bright band signatures in terms of polarimetric radar variables. This is in response to higher density particles that descend to lower altitudes before acquiring sufficient meltwater to produce polarimetric contrasts. For 27 April, although melting starts at a similar height along both spirals (for example, as marked by substantial increases in mean Doppler velocity from KAZR), complete melting (particles attaining raindrop fall speeds) does not occur until a lower altitude along Spiral 1 (Figure 9a). The height of the RWP bright band Z maximum along Spiral 1 is also lower than along Spiral 2 (e.g., Figure 9c). The RWP Z maximum is also substantially weaker along Spiral 1 than observed during Spiral 2 (Figure 9b). These column melting layer signatures are consistent with the findings of those previous studies.

During Spiral 1, the smaller disdrometer  $D_m$  values (Figure 1e) are in modest agreement with the expectations for riming, smaller aggregates associated with weaker bright band signatures, and/or smaller mean raindrop sizes (absence of larger aggregates). Larger surface  $D_m$  values throughout the downward spiral are linked to larger snowflake aggregation and the propensity for these larger melting snowflakes to lead to larger mean drop sizes (neglecting potential coalescence or breakup beneath the melting layer). The changeover at 10:50 UTC is lag correlated (approximately 25 min) with the suspected influx of larger ice aloft and possibly physically reasonable for the transition toward more prominent, larger particles, and time associated with larger aggregates to reach the surface. However, correlations with surface disdrometer estimates should be interpreted with caution. Linear and rank lag correlations between bright band parameters (e.g., maximum Z, mean Doppler velocity difference between Ka and RWP wavelengths) and surface  $D_m$  and rainfall rates, typically do not exceed  $r=0.6$ .

### 3.2.3. Additional Profiling Instrument Interpretation: Ice Needles

Vogel *et al.* [2015] proposed that stratiform or widespread precipitation may contain riming regions that also feature strong Doppler spectral bimodalities in profiling radar observations. These bimodalities would be indicative of rimed particles coincident with additional slower falling plates or needles. The most pronounced radar signature contrasts we observe during this 27 April 2011 event are those from a significant spectral bimodality along the Spiral 1. It is interesting to contrast radar behaviors along Spiral 2 to Spiral 1 (Figures 10 and 11), since KAZR spectra along Spiral 2 display no obvious bimodalities, with weaker evidence for riming or supercooled liquid water as from Citation probe interpretations. The bimodality we observe in Figures 10a and 10b is consistent with ice because both peaks demonstrate strong spectral cross-polar returns and appropriate ice melting behaviors when reaching the melting level. These features are also captured by a prolonged, deeper spectral skewness behaviors (Figure 1c), timed with aircraft riming signatures and a reduction in radar melting layer Z enhancements over the SGP CF from the RWP (Figure 9c). Although spectral skewness is found to decrease with rimed or riming particles, the most pronounced change to the skewness is seen with the addition of slower falling ice needles.

Further, Vogel *et al.* [2015] suggest that bimodal spectra are useful to indicate that riming is occurring. For the 27 April event, the KAZR spectragrams and coupled aircraft insights strongly indicate riming and supercooled liquid for regions above but potentially also overlapping with those having bimodal spectra. Since we interpret from section 3.1 that the conditions favorable for riming are also those conducive to generate the embryonic ice at these altitudes necessary for ice needles, it may also follow that locating two-ice bimodal signatures implies that riming is occurring somewhere in proximity of those bimodal spectra observations (radar-based proxy). However, the persistent and narrow layer exhibiting negative skewness that we observe for several hours prior (Figure 1c) and additional available LWC at appropriate altitudes (e.g., Figure 1d) suggests that these bimodal signatures or favorable conditions may also have been found far downstream from the ongoing and/or more pronounced riming process regions as argued along Spiral 1.

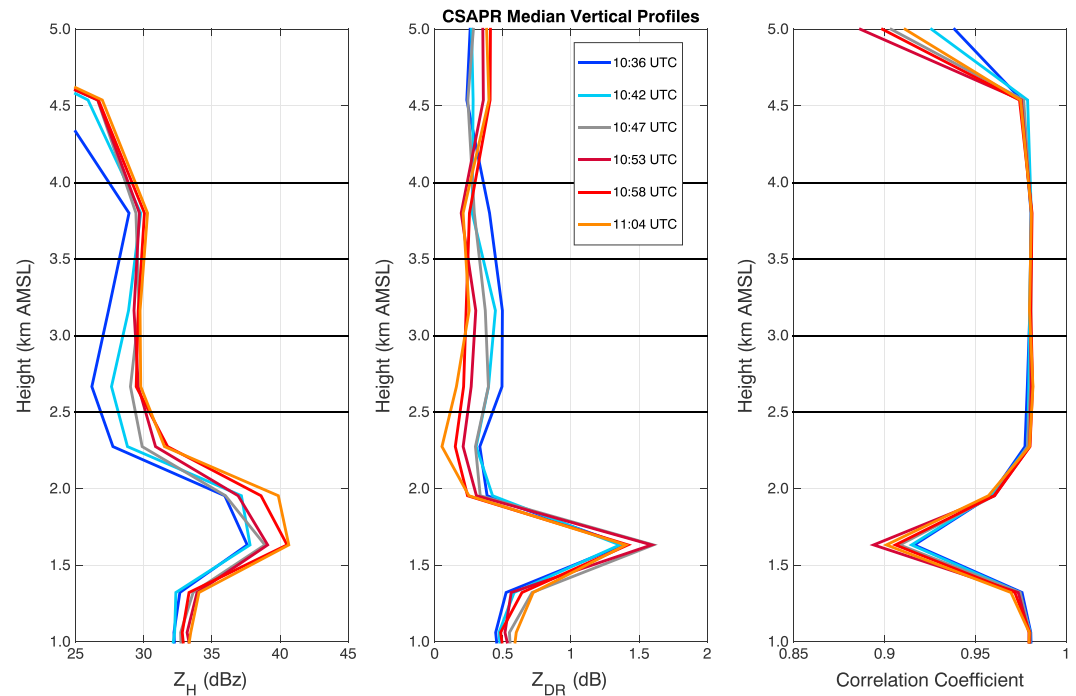


**Figure 12.** Median CSAPR vertical profiles for  $Z$ ,  $Z_{DR}$ , and cross-correlation coefficient for a narrow sector over the SGP CF on the 27 April 2011 event. CSAPR volumes are color coded in time to mark the transition from Spiral 1 (bluer colors) toward Spiral 2 (red, warmer colors).

### 3.3. ARM CSAPR: Observations and Interpretation Supported by Aircraft

For this study, dual polarization radar responses to the microphysical process differences suggested between the spirals by aircraft and supported by profiling radar explored by using median vertical profiles are constructed from multiple PPI scans collected from the CSAPR (Figure 12). These plots are generated by considering radar data from the narrow 5 km in range and  $13^\circ$  azimuth sector over the SGP CF location that contained the Citation spiral. Figure 12 plots the median  $Z$ ,  $Z_{DR}$ , and copolar correlation coefficient profiles from each CSAPR volume collected during the spiral sequence. The CSAPR volumes are color coded in time to mark the transition from Spiral 1 (cold, blue colors) toward Spiral 2 (warm, red colors).

Traditionally, aggregation as viewed by longer-wavelength dual polarization radars is often associated with an increase in  $Z$  and decrease in  $Z_{DR}$  profiles toward the melting level. These radar signatures are accompanied by low values for  $Z_{DR}$  (near 0.2 dB) just above the melting level. Such behaviors would be consistent with larger aggregates having lower effective density and increased dispersion of canting angles [e.g., Giangrande et al., 2008; Kumjian et al., 2014]. In contrast, riming profiles as viewed by dual polarization radars in traditional deeper convective contexts may span a range of  $Z$  values; however, riming regions have tended to be associated with low  $Z_{DR}$  as a consequence of more spherical, rimed particle shapes and/or the falling behaviors for these anisotropic scatterers. More recently, scattering calculations performed by Vogel et al. [2015] have proposed that riming embedded within stratiform precipitation may include varied responses in dual polarization radar measurements contingent on the presence of bimodal Doppler spectra and degree of riming. From the previous sections, Citation and profiling radar observations indicate that the 27 April event featured strong multisensor evidence for riming over the SGP CF, with collocated rimed particles and pristine needles below 3.5–4 km. High concentrations of pristine needles mixed with rimed particles might not substantially increase  $Z$  when viewed by longer-wavelength radars (which is dominated by the larger rimed particles) as from RWP profiles (Figure 9c), but these needles may act to increase the overall  $Z_{DR}$ . The additional diversity of particle shapes can also lower the copolar correlation coefficient [e.g., Andric et al., 2013; Vogel et al., 2015].

Longer-wavelength CSAPR  $Z$  profile magnitudes are found to be lower aloft at earlier times, with  $Z$  gradually increasing in response to an increasing number of larger particles with time, as also informed by the RWP and aircraft. Coincident with needle locations and adjacent to possible riming locations identified along Spiral 1,

Figure 12 indicates a relative increase in  $Z_{DR}$  aloft (0.2 to 0.4 dB). This is in good agreement with having pristine needle concentrations and expectations from modeling performed in *Vogel et al.* [2015]. Similar to RWP profiles, CSAPR profile melting layer enhancements are reduced during the earlier conditions favorable for riming aloft, with  $Z$  enhancements gradually increasing before 11:00 UTC when the Citation confirms ongoing aggregation with additional presence of larger aggregates.

Unlike KAZR and RWP profiles in Figures 9–11 that feature superior vertical resolution, the median CSAPR profiles reconstructed from PPI scans provide no direct evidence that the onset of melting or bright band parameters such as  $Z$  or  $Z_{DR}$  peak locations are significantly offset between riming favorable and later periods. Such differences in bright band characteristics are perhaps only detectable when alternative data interrogation techniques are used, such as the quasi-vertical profile method that may provide improved vertical resolution [e.g., *Ryzhkov et al.*, 2016; *Kumjian et al.*, 2016]. Similar to profiler observations, linear and rank lag correlations with surface  $D_m$  and rainfall rates did not exceed  $r = 0.6$ . Again, riming periods aloft are loosely associated with smaller raindrop sizes, an absence of larger aggregates (although not an absence of aggregation). However, these relationships are additionally complex as evident in Figure 12 with an indication that the maximum  $Z$  and  $Z_{DR}$  in the bright band are temporally offset (11:04 UTC and 10:53 UTC, respectively) during the event.

#### 4. Key Findings and Summary

This study documents aircraft spiral and radar observations for a transition from riming conditions to possible larger particle and aggregation favorable conditions in a widespread stratiform precipitation event. Capturing the conditions when and where processes including riming and aggregation are active or dominant from remote sensing platforms is critical for future convective model improvement. Process signatures were fortuitously captured during a MC3E event during which aircraft spiral data sets were collected over the ARM surface supersite. Profiling radar observations first drew our attention to the event; these observations include interesting Doppler spectral peak changes in time and height, higher particle fall speeds, and reduced, sagging radar bright band signatures that accompany passage of a riming region in a stratiform field. Analyses of Citation aircraft spirals through this period support riming aloft with measurements of increased LWC, PSDs with spherical shapes, and supersaturation with respect to water to  $-15^{\circ}\text{C}$ . The coincident, multisensor aircraft and radar approach provided confidence in our capture of riming processes, with KAZR-based spectral signatures informative to isolate riming particles and likely riming regions for this event. Radar capabilities to identify aggregation processes were also explored, with results highlighting the importance for multiwavelength and spectral based radar methods that may better sample the behaviors over a range of particle sizes.

Bimodal Doppler spectra are also observed to originate near riming regions and are associated with pristine needles between  $-4^{\circ}\text{C}$  and  $-7^{\circ}\text{C}$ . The needles are observed by Citation probes, KAZR spectragrams, and bulk changes in dual polarization radar variables. The evidence suggests that these crystals are pristine when observed near the strongest riming signatures, arguing for possible secondary ice production in close spatiotemporal proximity to these conditions. Analysis of CSAPR dual polarization fields suggests that these needles, when collocated with spherical rimed particles, may act to increase bulk  $Z_{DR}$  by 0.2–0.4 dB. It is interesting that according to previous *Ryzhkov et al.* [2016] and *Kumjian et al.* [2016] studies, heavy riming of snow is usually accompanied by an increase in  $Z$  and a decrease of  $Z_{DR}$ , similar to the expectations for embedded convection. However, in cases of weaker riming when the contribution of secondary and highly anisotropic ice (e.g., needles) to the radar reflectivity is comparable to the one from primary, quasi-spherical rimed snow,  $Z_{DR}$  can be 0.2–0.3 dB higher than that of dry, unrimed aggregates. These statements are confirmed in this study, as in the recent work of *Vogel et al.* [2015]. As the event progressed, dual polarization radar signatures eventually transitioned toward traditional profile expectations consistent with aggregation of larger snowflakes.

Melting layer behaviors along Spiral 1 highlight a mixture of melting smaller ice particles and rimed particles, resulting in a delayed and weaker melting layer signature [e.g., *Kumjian et al.*, 2016]. The more pronounced bright band signatures are associated with Spiral 2 having additional larger melting aggregates entering the melting layer and fewer rimed particles (deposition dominating riming aloft, larger snow particles overall, and aggregation for those particles). Aggregation is observed along both spirals, but larger aggregates generated and/or propagated along Spiral 2 lead to larger surface  $D_m$ . The Spiral 1 riming-dominant profile conditions and smaller aggregates and melting rimed particles are associated with smaller relative surface  $D_m$ .

## Acknowledgments

This manuscript has been authored by employees of Brookhaven Science Associates, LLC under contract DE-AC02-98CH10886 with the U.S. Department of Energy. Bansemer was partially supported by DOE ASR grant DE-SC0008648. The publisher by accepting the manuscript for publication acknowledges that the United States Government retains a nonexclusive, paid-up, irrevocable, worldwide license to publish or reproduce the published form of this manuscript, or allow others to do so, for United States Government purposes. Financial support for A. Ryzhkov, M. Kumjian, and S. Mishra was provided through the grant ER65459 from the U.S. Department of Energy Atmospheric System Research Program and from NOAA Office of Atmospheric Research under NOAA University of Oklahoma Cooperative Agreement NA11OAR4320072, U.S. Department of Commerce. The authors wish to thank the ARM Climate Research Facility for the extended KAZR, disdrometer, CSAPR, and RWP data sets (Instrument mentors Nitin Bharadwaj, Scott Collis, Mary Jane Bartholomew, and Richard Coulter) collection, products and maintenance, and the crew and scientists of the University of North Dakota Citation aircraft. Special thanks also to David Delene (UND) for his helpful discussions on the Citation probes and their uncertainties. We would also like to thank the efforts of Edward Luke, Karen Johnson, Michael Jensen, Isztar Zawadzki, and Mariko Oue for ARM KAZR moment and Doppler spectral processing products and associated discussions on spectral signatures.

## References

- Ackerman, T. P., and G. M. Stokes (2003), The atmospheric radiation measurement program, *Phys. Today*, 39–44.
- Andric, J., M. R. Kumjian, D. S. Zrnica, J. M. Straka, and V. M. Melnikov (2013), Polarimetric signatures above the melting layer in winter storms: An observational and modeling study, *J. Appl. Meteorol. Climatol.*, 52, 682–700.
- Atmospheric Radiation Measurement (ARM) Climate Research Facility (2006), Updated daily. Impact Disdrometer (DISDROMETER). 2011-04-27, 36.605 N 97.485 W: Southern Great Plains (SGP) Central Facility, Lamont, OK (C1), Compiled by M. Bartholomew. Atmospheric Radiation Measurement (ARM) Climate Research Facility Data Archive: Oak Ridge, Tenn. [Available at 10.5439/1025181.]
- Atmospheric Radiation Measurement (ARM) Climate Research Facility (2009), Updated hourly, Radar Wind Profiler (915RWP/PRECIPMOM). Compiled by R. Coulter, T. Martin and P. Muradyan. Atmospheric Radiation Measurement (ARM) Climate Research Facility Data Archive: Oak Ridge, Tenn. [Available at 10.5439/1025128.]
- Atmospheric Radiation Measurement (ARM) Climate Research Facility (2010), Updated hourly. C-Band ARM Precipitation Radar (CSAPRSUR). Compiled by N. Bharadwaj, D. Nelson, B. Isom, J. Hardin, I. Lindenmaier and S. Collis. Atmospheric Radiation Measurement (ARM) Climate Research Facility Data Archive: Oak Ridge, Tenn. [Available at 10.5439/1025170.]
- Atmospheric Radiation Measurement (ARM) Climate Research Facility (2011), Updated hourly, Ka ARM Zenith Radar (KAZRSPECCMASKGECOPOL). Compiled by N. Bharadwaj, D. Nelson, B. Isom, J. Hardin, I. Lindenmaier and K. Johnson. Atmospheric Radiation Measurement (ARM) Climate Research Facility Data Archive: Oak Ridge, Tenn. [Available at 10.5439/1025218.]
- Battaglia, A., S. Tanelli, and P. Kollias (2013), Polarization diversity for millimeter spaceborne Doppler radars: An answer for observing deep convection? *J. Atmos. Oceanic Technol.*, 30, 2768–2787.
- Baumgardner, D., and A. Rodi (1989), Laboratory and wind tunnel evaluations of the Rosemount icing detector, *J. Atmos. Oceanic Technol.*, 6, 971–979.
- Bailey, M. P., and J. Hallett (2009), A comprehensive habit diagram for atmospheric ice crystals: Confirmation from the laboratory, AIRS II, and other field studies, *J. Atmos. Sci.*, 66, 2888–2899, doi:10.1175/2009JAS2883.1.
- Bellon, A., I. Zawadzki, and F. Fabry (1997), Measurements of melting layer attenuation at X-band frequencies, *Radio Sci.*, 32(3), 943–955, doi:10.1029/97RS00492.
- Bringi, V. N., G. Huang, V. Chandrasekar, and E. Gorgucci (2002), A methodology for estimating the parameters of a gamma raindrop size distribution model from polarimetric radar data: Application to a squall-line event from the TRMM/Brazil campaign, *J. Atmos. Oceanic Technol.*, 4, 464–478.
- Bringi, V. N., V. Chandrasekar, J. Hubbert, E. Gorgucci, W. L. Randeu, and M. Schoenhuber (2003), Raindrop size distribution in different climatic regimes from disdrometer and dual polarized radar analysis, *J. Atmos. Sci.*, 60, 354–365.
- Clothiaux, E. E., T. P. Ackerman, G. G. Mace, K. P. Moran, R. T. Marchand, M. A. Miller, and B. E. Martner (2000), Objective determination of cloud heights and radar reflectivities using a combination of active remote sensors at the ARM CART sites, *J. Appl. Meteorol.*, 39, 645–665.
- Fabry, F., and I. Zawadzki (1995), Long-term radar observations of the melting layer of precipitation and their interpretation, *J. Atmos. Sci.*, 52, 838–851.
- Fletcher, N. H. (1962), *The Physics of Rainclouds*, pp. 386, Cambridge Univ. Press, Cambridge.
- Fukuta, N., and R. C. Schaller (1982), Ice nucleation by aerosol particles. Theory of condensation-freezing nucleation, *J. Atmos. Sci.*, 39, 648–655.
- Giangrande, S. E., J. M. Krause, and A. V. Ryzhkov (2008), Automatic Designation of the Melting Layer with a Polarimetric Prototype of the WSR-88D Radar, *J. Appl. Meteorol. Climatol.*, 47, 1354–1364.
- Giangrande, S. E., E. P. Luke, and P. Kollias (2010), Automated retrievals of precipitation parameters using non-Rayleigh scattering at 95 GHz, *J. Atmos. Oceanic Technol.*, 27, 1490–1503.
- Giangrande, S. E., S. Collis, J. Straka, A. Protat, C. Williams, and S. Krueger (2013), A summary of convective-core vertical velocity properties using ARM UHF wind profilers in Oklahoma, *J. Appl. Meteorol. Climatol.*, 52, 2278–2295.
- Giangrande, S. E., M. J. Bartholomew, M. Pope, S. Collis, and M. P. Jensen (2014a), A summary of precipitation characteristics from the 2006–11 northern Australian wet seasons as revealed by ARM disdrometer research facilities (Darwin, Australia), *J. Appl. Meteorol. Climatol.*, 53, 1213–1231.
- Giangrande, S. E., S. Collis, A. K. Theisen, and A. Tokay (2014b), Precipitation estimation from the ARM distributed radar network during the MC3E campaign, *J. Appl. Meteorol. Climatol.*, 53, 2130–2147.
- Giangrande, S., E. P. Luke, and P. Kollias (2012), Characterization of vertical velocity and drop size distribution parameters in widespread precipitation at ARM facilities, *J. Appl. Meteorol. Climatol.*, 51, 380–391.
- Guyot, G., C. Gourbeyre, G. Febvre, V. Shcherbakov, F. Burnet, J.-C. Dupont, K. Sellegri, and O. Jourdan (2015), Quantitative evaluation of seven optical sensors for cloud microphysical measurements at the Puy-de-Dôme Observatory, France, *Atmos. Meas. Tech.*, 8, 4347–4367, doi:10.5194/amt-8-4347-2015.
- Hallett, J., and S. C. Mossop (1974), Production of secondary ice particles during the riming process, *Nature*, 249, 26–28, doi:10.1038/249026a0.
- Heymsfield, A. J., and C. D. Westbrook (2010), Advances in the estimation of ice particle fallspeeds using laboratory field measurements, *J. Atmos. Sci.*, 67, 2469–2482.
- Heymsfield, A. J., A. Bansemer, M. R. Poellot, and N. Wood (2015), Observations of ice microphysics through the melting layer, *J. Atmos. Sci.*, doi:10.1175/JAS-D-14-0363.1.
- Heymsfield, A., and P. Willis (2014), Cloud conditions favoring secondary ice particle production in tropical maritime convection, *J. Atmos. Sci.*, 71, 4500–4526.
- Heymsfield, A., and S. C. Mossop (1984), Temperature dependence of secondary ice crystal production during soft hail growth by riming, *Q. J. R. Meteorol. Soc.*, 110, 765–770, doi:10.1002/qj.49711046512.
- Hou, A. Y., R. K. Kakar, S. Neeck, A. A. Azarbarzin, C. D. Kummerow, M. Kojima, R. Oki, K. Nakamura, and T. Iguchi (2014), The global precipitation measurement (GPM) mission, *Bull. Am. Meteorol. Soc.*, 95(5), 701–722, doi:10.1175/BAMS-D-13-00164.1.
- Illingworth, A. J., et al. (2007), Cloudnet: Continuous evaluation of cloud profiles in seven operational models using ground based observations, *Bull. Am. Meteorol. Soc.*, 88, 883–898.
- Jensen, M. P., T. Toto, D. Troyan, P. Ciesielski, D. Holdridge, J. Kyrouac, J. Schatz, Y. Zhang, and S. Xie (2015a), The MC3E sounding network: Operations, processing, and analysis, *Atmos. Meas. Tech.*, 8, 421–434, doi:10.5194/amt-8-1-2015.
- Jensen, M., et al. (2015b), The Midlatitude Continental Convective Clouds Experiment (MC3E), *Bull. Am. Meteorol. Soc.*, doi:10.1175/BAMS-D-14-00228.1.
- Joss, J., and A. Waldvogel (1967), A raindrop spectrograph with automatic analysis, *Pure Appl. Geophys.*, 68, 240–246.

- Kalesse, H., W. Szyrmer, S. Kneifel, P. Kollias, and E. Luke (2016), Fingerprints of a riming event on cloud radar Doppler spectra: Observations and modeling, *Atmos. Chem. Phys.*, *16*, 2997–3012, doi:10.5194/acp-16-2997-2016.
- Khelif, D., S. P. Burns, and C. A. Friehe (1999), Improved wind measurements on research aircraft, *J. Atmos. Oceanic Technol.*, *16*, 860–875.
- Knight, C. (2012), Ice growth from the vapor at  $-5^{\circ}\text{C}$ , *J. Atmos. Sci.*, *69*, 2031–2040.
- Knollenberg, R. G. (1981), Techniques for probing cloud microstructure, in *Clouds, Their Formation, Optical Properties, and Effects*, pp. 15–91, Academic Press, New York.
- Kobayashi, T. (1961), The growth of snow crystals at low supersaturations, *Philos. Mag.*, *6*, 1363–1370.
- Kollias, P., E. E. Clothiaux, A. A. Miller, B. A. Albrecht, G. L. Stephens, and T. P. Ackerman (2007), Millimeter-wavelength radars: New frontier in atmospheric cloud and precipitation research, *Bull. Am. Meteorol. Soc.*, *88*, 1608–1624, doi:10.1175/BAMS-88-10-1608.
- Kollias, P., J. Rémillard, E. Luke, and W. Szyrmer (2011), Cloud radar Doppler spectra in drizzling stratiform clouds: 1. Forward modeling and remote sensing applications, *J. Geophys. Res.*, *116*, D13201, doi:10.1029/2010JD015237.
- Kollias, P., N. Bharadwaj, K. Widener, I. Jo, and K. Johnson (2014), Scanning ARM cloud radars. Part I: Operational sampling strategies, *J. Atmos. Oceanic Technol.*, *31*, 569–582.
- Kumjian, M., and A. V. Ryzhkov (2010), The impact of evaporation on polarimetric characteristics of rain: Theoretical model and practical implications, *J. Appl. Meteorol. Climatol.*, *49*, 1247–1267.
- Kumjian, M., and A. V. Ryzhkov (2012), The impact of size sorting on the polarimetric radar variables, *J. Atmos. Sci.*, *69*, 2042–2060.
- Kumjian, M., and O. P. Prat (2014), The impact of raindrop collisional processes on the polarimetric radar variables, *J. Atmos. Sci.*, *71*, 3052–3067.
- Kumjian, M. R., S. Mishra, S. E. Giangrande, T. Toto, A. V. Ryzhkov, and A. Bansemer (2016), Polarimetric radar and aircraft observations of saggy bright bands during MC3E, *J. Geophys. Res. Atmos.*, *121*, 3584–3607, doi:10.1002/2015JD024446.
- Kumjian, M., S. M. Ganson, and A. V. Ryzhkov (2012), Freezing of raindrops in deep convective updrafts: A microphysical and polarimetric model, *J. Atmos. Sci.*, *69*, 3471–3490.
- Kumjian, M., S. Rutledge, R. Rasmussen, P. Kennedy, and M. Dixon (2014), High-resolution polarimetric radar observations of snow-generating cells, *J. Appl. Meteorol. Climatol.*, *53*, 1636–1658.
- Lawson, R. P., R. E. Stewart, and L. J. Angus (1998), Observations and numerical simulations of the origin and development of very large snowflakes, *J. Atmos. Sci.*, *55*, 3209–3229.
- Lhermitte, R. (1988), Observations of rain at vertical incidence with a 94 GHz Doppler radar: An insight of Mie scattering, *Geophys. Res. Lett.*, *15*, 1125–1128, doi:10.1029/GL015i010p01125.
- Luke, E. P., and P. Kollias (2013), Separating cloud and drizzle radar moments during precipitation onset using Doppler spectra, *J. Atmos. Oceanic Technol.*, *30*, 1656–1671.
- Mather, J. H., and J. W. Voyles (2013), The arm climate research facility: A review of structure and capabilities, *Bull. Am. Meteorol. Soc.*, *94*, 377–392.
- Oue, M., M. R. Kumjian, Y. Lu, J. Verlinde, K. Aydin, and E. E. Clothiaux (2015), Linear depolarization ratios of columnar ice crystals in a deep precipitating system over the arctic observed by zenith-pointing Ka-band Doppler radar, *J. Appl. Meteorol. Climatol.*, *54*, 1060–1068.
- Rosenberg, P. D., A. R. Dean, P. I. Williams, J. R. Dorsey, A. Minikin, M. A. Pickering, and A. Petzold (2012), Particle sizing calibration with refractive index correction for light scattering optical particle counters and impacts upon PCASP and CDP data collected during the Fennec campaign, *Atmos. Meas. Tech.*, *5*, 1147–1163, doi:10.5194/amt-5-1147-2012.
- Ryzhkov, A. V., S. E. Giangrande, A. P. Khain, M. Pinsky, and A. Pokrovsky (2008), Exploring model-based polarimetric retrieval of vertical profiles of precipitation, fifth European Conf. on Radar in Meteor. and Hydrol., Helsinki, Finland, FMI, CD ROM, P6.1.
- Ryzhkov, A. V., M. Pinsky, A. Pokrovsky, and A. Khain (2011), Polarimetric radar observation operator for a cloud model with spectral microphysics, *J. Appl. Meteorol. Climatol.*, *50*, 873–894.
- Ryzhkov, A. V., M. R. Kumjian, S. M. Ganson, and A. P. Khain (2013), Polarimetric radar characteristics of melting hail. Part I: Theoretical simulations using spectral microphysical modeling, *J. Appl. Meteorol. Climatol.*, *52*, 2849–2870.
- Ryzhkov, A. V., P. Zhang, H. D. Reeves, M. R. Kumjian, T. Tschallener, S. Tromel, and C. Simmer (2016), Quasi-vertical profiles: A new way to look at polarimetric radar data, *J. Atmos. Oceanic Technol.*, *33*, 551–561.
- Sassen, K., J. R. Campbell, J. Zhu, P. Kollias, M. Shupe, and C. Williams (2005), Lidar and triple-wavelength Doppler radar measurements of the melting layer: A revised model for dark and bright band phenomena, *J. Appl. Meteorol.*, *44*, 301–312.
- Stewart, R. E., J. D. Marwitz, J. C. Pace, and R. E. Carbone (1984), Characteristics through the melting layer of stratiform clouds, *J. Atmos. Sci.*, *41*(22), 3227–3237.
- Stokes, G. M., and S. E. Schwartz (1994), The Atmospheric Radiation Measurement (ARM) program: Programmatic background and design of the cloud and radiation test bed, *Bull. Am. Meteorol. Soc.*, *75*, 1201–1221.
- Takahashi, T., Y. Nagao, and Y. Kushiya (1995), Possible high ice particle production during Graupel–Graupel collisions, *J. Atmos. Sci.*, *52*, 4523–4527.
- Tokay, A., W. A. Petersen, P. Gatlin, and M. Wingo (2013), Comparison of raindrop size distribution measurements by collocated disdrometers, *J. Atmos. Oceanic Technol.*, *30*, 1672–1690.
- Vogel, J. M., F. Fabry, and I. Zawadzki (2015), Attempts to observe polarimetric signatures of riming in stratiform, *Preprints*, 37<sup>th</sup> Conference on Radar Meteorology, Norman, Okla.
- Wang, J., X. Dong, and B. Xi (2015), Investigation of ice cloud microphysical properties of DCSs using aircraft in situ measurements during MC3E over the ARM SGP site, *J. Geophys. Res. Atmos.*, *120*, 3533–3552.
- White, A., D. J. Gottas, E. T. Strem, F. M. Ralph, and P. J. Neiman (2002), An automated bright band height detection algorithm for use with Doppler radar spectral moments, *J. Atmos. Oceanic Technol.*, *19*, 687–697.
- Williams, C. (2012), Vertical air motion retrieved from dual frequency profiler observations, *J. Atmos. Oceanic Technol.*, *29*, 1471–1480.
- Willis, P., and A. J. Heymsfield (1989), Structure of the melting layer in mesoscale convective system stratiform precipitation, *J. Atmos. Sci.*, *46*, 2008–2025.
- Zawadzki, I., F. Fabry, and W. Szyrmer (2001), Observations of supercooled water and of secondary ice generation by a vertically pointing X-band Doppler radar, *Atmos. Res.*, *59–60*, 343–359.